Computers and Structures 120 (2013) 9–23

Contents lists available at SciVerse ScienceDirect

Computers and Structures

journal homepage: www.elsevier.com/locate/compstruc

A three-dimensional cyclic meso-scale numerical procedure for simulation of unreinforced masonry structures

Amjad J. Aref*, Kiarash M. Dolatshahi

Department of Civil, Structural and Environmental Engineering, University at Buffalo, The State University of New York, NY, USA

ARTICLE INFO

Article history:
Received 6 February 2012
Accepted 21 January 2013
Available online 6 March 2013

Keywords:
Masonry
Three-dimensional modeling
Explicit procedure
Cyclic modeling
Dynamic
Constitutive material model

ABSTRACT

Three-dimensional (3D) cyclic analysis and constitutive material model are needed to better understand the behavior of unreinforced masonry (URM) buildings under earthquake excitations. So far, most of the existing constitutive material models applied to the field of masonry structures have focused on two-dimensional modeling and monotonic loading. In addition, most of the studies have used implicit dynamic procedures in the time domain. Based on the inherent features of implicit formulations for non-linear problems, a number of iterations are required at each time step to achieve convergence, which leads to intensive computations and lack of convergence in some cases such as cyclic loadings.

In this paper, a 3D cyclic constitutive material model implemented within an explicit analysis procedure is proposed, which can be used to model large deformation behavior of masonry walls. A rigorous constitutive material model is proposed and validated with available experimental data from previous researches, and for the attributes for which experimental data is not readily available; a number of new experimental tests has been conducted by the authors. The material model is implemented in a user-defined subroutine and compiled with ABAQUS (VUMAT). The subroutine is then tested by several numerical examples on a single element under cyclic normal and transverse deformations to examine the behavior of the material model. Moreover, several analyses are conducted and the numerical results are compared with experimental data to assess the robustness and predictive capabilities of the proposed material model and the numerical solution algorithms.

1. Introduction

Masonry structures have been used for many years in building construction. The poor performance of masonry buildings under earthquake excitations has been observed over the years; however, masonry buildings are still in demand. Although novel structural technologies are utilized in new buildings, masonry components are not omitted from structural usage, and masonry components are still used especially as infill walls, whereby they provide significant stiffness to buildings in earthquakes. Whether the masonry structure constitutes the whole structural system or used as infill walls in a concrete or steel building, the complex failure modes often pose a significant challenge for any computational framework. Therefore, it is necessary to develop new and robust material models capable of capturing the cyclic three dimensional behavior of unreinforced masonry structures. An extensive literature review of existing approaches to modeling masonry structures reveals that few detailed material models and analysis strategies exist, and those that are available primarily focus on investigating the two-dimensional (2D) cyclic behavior of masonry components and structures [3–7].

Based on the sought accuracy level, different types of computational methods, with varying levels of computational demand, have been presented to assess the behavior of masonry structures under static and dynamic loadings [1,2,8,9]. These computational methods are mainly categorized into three groups—namely, micro-, macro-, and meso-scale. In micro-scale modeling approach, each part of the wall is modeled in detail, using finite element method (FEM), and that consequently provides a high level of accuracy for fine meshes and appropriate material models; however, the time to create a complete numerical model and the analysis computational demand are very significant and in many cases is prohibitive if large scale computational resources are not available. Accordingly, for practical purposes, meso- and macro-level analyses have become the most common methods for studying the structural response of masonry structures. In macro-scale analysis, usually the general behavior of components is the main point of interest. These types of models are much easier to use than the micro-scale methods in terms of generating the idealized numerical model and analyzing the structural system. Therefore, macro-scale approaches are preferred for large structures and particularly for seismic analysis. In a nutshell, the macro-scale

* Corresponding author. Tel.: +1 716 6454369; fax: +1 716 645 3733.
E-mail addresses: aaref@buffalo.edu (A.J. Aref), km256@buffalo.edu (K.M. Dolatshahi).

0045-7949/$ - see front matter © 2013 Elsevier Ltd. All rights reserved.
http://dx.doi.org/10.1016/j.compstruc.2013.01.012

Nomenclature

a, t and h	width, thickness and height of wall, respectively
k_n	normal stiffness of joints
$k_{sx,y}$	transverse stiffness of joints
$\tan\phi$	friction coefficient
$\tan\psi$	dilatancy coefficient
ϕ_0	initial friction angle
ϕ_r	residual friction angle
f_c	compressive strength of brick
f_t	tensile strength
c	shear strength
G_f^I	tensile softening energy
G_f^{II}	shear softening energy
E_m, E_b	mortar and brick modulus of elasticity
G_m, G_b	mortar and brick shear modulus
h_m, h_b	mortar and brick height
σ	normal stress
τ	shear stress
u_n	normal displacement
u_s	shear displacement
κ_1/κ_t	stiffness degradation factor

analysis is associated with many simplified assumptions to significantly reduce the computational time. For example, Pasticier et al. [10] used a very simple macro-element model to perform two-dimensional seismic analysis of masonry panels, where each part was divided into smaller panels that were represented by an equivalent beam element with predefined hysteretic behavior.

As another example for macro-scale analysis of masonry buildings, Chen et al. [11] used nonlinear shear springs in series with rotational springs to simulate both shear and flexural in-plane response of masonry walls. The proposed macro-element includes an axial spring, three shear springs, and two rotational springs to simulate the behavior of masonry walls. Using large rigid elements and springs attached between them, Casolo [12] developed a macro-scale model where he compared the frequencies and mode shapes of a masonry wall using his proposed model and finite element model. Later the model was extended to capture the cyclic 2D behavior of masonry walls and to model masonry walls under earthquake excitations [6]. In the model proposed by Casolo, the propagated cracks of the wall were represented by a damage parameter. Park et al. [8] proposed a model in which a masonry panel was divided into a number of springs with different hysteresis loops. Their model was effectively used to calculate the fragility curves for masonry structures. In addition to the studies described herein, many macro-model approaches are available in literature, and for thorough review of these methods, we direct the reader to Dolatshahi's study [13].

In terms of the accuracy level and computational demand, meso-scale modeling is somewhere between micro- and macro-scale analysis. As an example of the early work on meso-scale modeling of masonry structures, Page [14] suggested using interface elements between bricks. The yield surface in this particular interface model is only defined for tensile and shear failure. Lourenco [1] subsequently modified Page's model by adding a compressive cap to the yield surface, which led to accounting for crushing of the masonry bricks. Oliveira and Lourenco [2] later generalized Lourenco's model to allow for the assessment of the cyclic behavior of masonry walls subjected to in-plane loading. In the model proposed by Lourenco [1] and later by Oliveira and Lourenco [2], bricks are modeled using elastic elements, and the nonlinear behavior of the interface elements includes the tensile, shear and compression failures [1]. In other words, all nonlinearity of the model is defined in the interface elements and all other elements in the model are assumed to remain elastic. Using rigid elements in combination with interface elements Dolatshahi and Aref [15] presented a meso-scale numerical model for simulation of crack propagation in unreinforced masonry walls. Using rigid elements that replaced solid elements in the FEM have led to significantly decreasing the number of degrees-of-freedom (DOF) of the system and alleviating the computational demand while producing a good agreement with experimentally obtained data.

With respect to the temporal discretization, micro- and meso-scale analysis can follow either implicit or explicit procedures. Most of the notable research studies that address cyclic behavior of masonry structures use implicit finite element solutions. Modeling a masonry structure with an implicit procedure offers some advantages as well as many technical challenges. Based on the most fundamental characteristics of implicit procedures, at each time step, iterations are required to solve a system of equations. The behavior of masonry structures is inherently nonlinear; thus, an implicit procedure needs to iterate to achieve the desired convergence tolerance. Unfortunately, for highly nonlinear problems such as the one that represents a masonry structure, an implicit FEM solution often encounters convergence issues and termination of the solution at very early stages of the nonlinear regime. Most of the finite element codes used to analyze masonry structures are based on implicit formulations [1–3], and the analysis is computationally extensive when one considers large displacement domain. The convergence of the numerical solution particularly deteriorates at the point of load reversal [16]. For this reason researchers [17,18] have used explicit formulations to remedy the convergence problems. For example, Karapitta et al. [17] used a homogenization technique within an explicit formulation to capture the cyclic behavior of in-plane masonry panels. Although the homogenization model captured a significant range of the nonlinear behavior very well, it could not capture the creation and progression of discrete cracks. Instead, a damage parameter is used to show the distorted elements. It should be noted that there are also some disadvantages for explicit solutions. For instance, there is a risk of converging to wrong solutions since the equilibrium is not enforced. Moreover, the final result can be dependent to the selected time step and also many small time increments are needed which is time-consuming.

Based on an extensive literature review [13], the authors have found very few 3D cyclic finite element models that are readily available to accurately model the behavior of masonry structures. This paper presents a comprehensive study for 3D modeling of masonry structures, and is organized as follows; first, the description of the finite element model and any pertinent assumptions are presented, including the types of elements used to model the mortar and bricks. Second, the elastic and inelastic constitutive material models are described and accompanied with numerical examples used to validate a single element, to better illustrate and test the behavior of the proposed numerical procedures. Finally, the proposed numerical procedure is validated using experimental results under the in-plane monotonic, out-of-plane monotonic and combination of in-plane and out-of-plane cyclic loadings.

2. Description of the finite element model

In the proposed 3D finite element model, which is a meso-scale model, bricks and mortar are distinctly defined by two types of elements. For both types of elements linear and nonlinear behavior are defined separately to achieve a better level of accuracy. The finite element models are generated in ABAQUS [19] using solid elements (C3D8R) for modeling bricks and plane interface elements (COH3D8), as shown in Fig. 1, for mortar.

As illustrated in Fig. 2, bricks are expanded by half the mortar thickness and interface elements are located between the brick elements representing the mortar.

Experimental observations indicate [20–22] that, in monotonic and cyclic loading of masonry walls, cracks mostly pass through either the mortar joint or middle of the bricks. As it will be discussed in Section 2.3, elasto–plastic behavior is defined for the brick elements to capture their nonlinear behavior. However, to guarantee for the possibility of crack propagation within the bricks, each brick is divided into two parts and an interface element with the constitutive material properties of brick (potential crack) is placed at such particular interfaces (see Fig. 3). We note here the user may choose more of the potential crack location and that adds the accuracy of the solution.

The proposed numerical procedures are considered to be in the domain of meso-scale analysis, since the mortar is not defined in detail and is represented using zero thickness interface elements. It should be noted that, with the usage of the zero thickness interface element, distinction between the bond (brick–mortar interface) failure and mid-thickness mortar failure is lost. In the following sections, the linear and nonlinear behavior of the elements, and pertinent numerical implementations used in the FE analysis are described.

2.1. Elastic behavior of joints

The behavior of the interface elements is initially elastic, i.e., $\Delta \boldsymbol{t} = k\Delta\bar{\boldsymbol{u}}$, where k is the elastic stiffness of joints and is calculated using the properties of both the brick and mortar utilizing equations (1)–(3), and $\boldsymbol{t}$ is the traction vector, where σ is the normal traction and $\tau_{x,y}$ is the transverse tractions. The deformation vector is defined by $\bar{\boldsymbol{u}}$, where according to Eq. (3) u represents the normal deformation of the interface element, and v_x and v_y are the transverse deformations in the x and y directions, respectively. The change in the stress or displacement in each increment is defined by Δ.

$$k = \begin{bmatrix} k_n & 0 & 0 \\ 0 & k_{sx} & 0 \\ 0 & 0 & k_{sy} \end{bmatrix} \tag{1}$$

$$\boldsymbol{t} = \begin{Bmatrix} \sigma \\ \tau_x \\ \tau_y \end{Bmatrix} \tag{2}$$

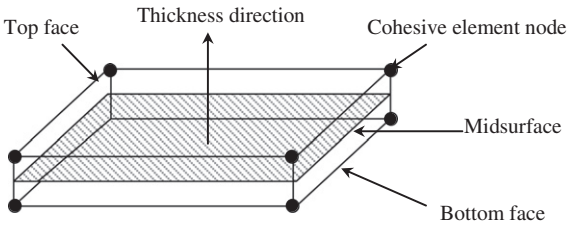

Fig. 1. Eight node plane interface element (ABAQUS).

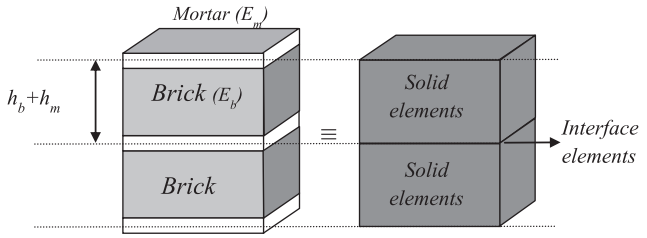

Fig. 2. Detailed model of brick and mortar.

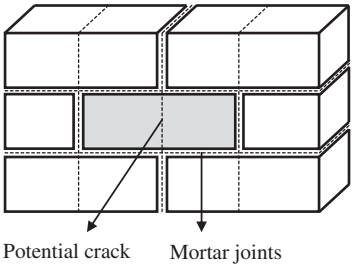

Fig. 3. Potential cracks.

$$\bar{\boldsymbol{u}} = \begin{Bmatrix} u \\ v_x \\ v_y \end{Bmatrix} \tag{3}$$

where k_n is the normal stiffness of the interface element and k_{sx} and k_{sy} are the transverse stiffness in the x and y directions, respectively. To determine the normal and shear stiffness, the brick and mortar are assumed to be elastic springs connected in series. The displacement for the combination of the brick and mortar system must be equal to the displacement of the brick element plane interface system under the same compressive and shear loads (Fig. 2). Accordingly, the stiffness of the system is calculated by using [1]

$$k_n = \frac{1}{h_m}\frac{E_m E_b}{E_b - E_m} \tag{4}$$

$$k_{sx,y} = \frac{1}{h_m}\frac{G_m G_b}{G_b - G_m} \tag{5}$$

where G is the shear modulus and the rest of parameters that appeared in Eqs. (4) and (5) are shown in Fig. 2. We note here that the subscripts "b" and "m" refer to brick and mortar, respectively. Following an explicit formulation, the displacement and strain increments at each time step are calculated first. Total displacements and strains in the new step $(i+1)$ are then generated by adding these increments to the displacements and strains obtained in the previous step (step i – Eq. (6)). The trial stress increments are calculated knowing the strain (or displacement) increments. However, to calculate the new stresses in step $i+1$ and before adding the stress increments to the stresses of step i, the state of stress must be checked to determine whether they are located in the elastic region or not (Eq. (7)). Section 2.2 addresses the case when the stresses are found to be outside of the yield surface.

$$\begin{aligned} u_{i+1} &= u_i + \Delta u \\ v_{x_{i+1}} &= v_{x_i} + \Delta v_x \\ v_{y_{i+1}} &= v_{y_i} + \Delta v_y \end{aligned} \tag{6}$$

$$\begin{cases} \sigma^{trial} = \sigma_i + \Delta u\ k_n \\ \tau_x^{trial} = \tau_{x_i} + \Delta v_x\ k_{sx} \\ \tau_y^{trial} = \tau_{y_i} + \Delta v_y\ k_{sy} \end{cases} \tag{7}$$

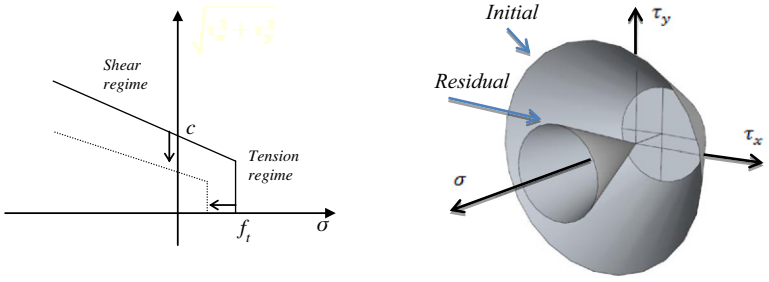

(a) Yield surface in 2D space (b) Yield surface in 3D space

Fig. 4. Yield surface for the joints.

where u, is the normal deformations relative to the interface element, and v_x and v_y are the transverse deformations in the x and y directions, respectively.

2.2. Plastic behavior of joints

Three distinct modes are considered for the interface elements namely, tension, shear, and tension-shear intersection (Fig. 4). As mentioned above, after calculating the trial stresses using Eq. (7), the status of the trial stresses must be checked with respect to all yield surfaces. If the state of stress in the step $i+1$ falls inside the yield surfaces, the material is in the linear regime and the trial stresses are correct. However, if the state of stress falls outside the yield surfaces, the stresses must be modified based on their respective plastic domain and that is to bring them to the yield surface.

$$\text{Linear Regime} \rightarrow \begin{cases} \text{If } \sigma^{trial} < \bar{\sigma}_1(\kappa_p) \\ \quad \text{for tension regime and} \\ \text{If } \sqrt{(\tau_x^{trial})^2 + (\tau_y^{trial})^2} < \sigma \tan\phi - \bar{\sigma}_2(\kappa_p) \\ \quad \text{for shear regime} \end{cases}$$

Each part of the yield surface of Fig. 4 is defined distinctly for tension, shear, and shear and tension regime in the following sections.

2.2.1. Tension regime

Exponential softening is considered for monotonic behavior of the joints in the tension domain following the work of Pluijm [23,24]. In the tension mode, the yield function [23] is

$$f_1(\sigma, \kappa_p) = \sigma - \bar{\sigma}_1(\kappa_p) \tag{8}$$

$$\bar{\sigma}_1 = f_t \exp\left(-\frac{f_t}{G_f^I}\kappa_p\right) \tag{9}$$

In Eqs. (8) and (9), f_t is the tensile strength of the brick–mortar interface and G_f^I is the mode-I fracture energy, which indicates the area under stress–displacement curve of a body under tensile force. κ_p is the plastic strain which, following an associated flow rule, in this case is equal to $|\Delta u^p|$ (increment of plastic normal displacement).

Following the normality rule [25], at any point of the yield surface the outward normal vector is proportional to the plastic strain increments. Moreover, while the material is in the nonlinear regime, at any particular time step, the stress state should remain on the yield surface. Therefore, Eq. (10) shows the stress correction factor which modifies the trial stresses.

$$\begin{cases} \frac{\partial f}{\partial \sigma} d\sigma + \frac{\partial f}{\partial \kappa_p} d\kappa_p = 0 \\ d\sigma = k\left(d\bar{\mathbf{u}} - d\lambda \frac{\partial f}{\partial \sigma}\right) \end{cases} \rightarrow d\lambda = \frac{-k_n du}{\frac{f_t^2}{G_f^I}\exp\left(-\frac{f_t}{G_f^I}\kappa_p\right) - k_n} \tag{10}$$

where k is defined in Eq. (1). By employing $d\lambda$, the new expression for the updated stresses becomes,

$$\begin{cases} \sigma_{i+1} = \sigma^{trial} - d\lambda\, k_n \\ \tau_{x_{i+1}} = \tau_x^{trial} \\ \tau_{y_{i+1}} = \tau_y^{trial} \end{cases} \tag{11}$$

Based on the experimental results, in the cyclic loadings the stiffness in each cycle degrades following the strength degradation [26,27]. To account for the stiffness degradation, at each cycle the ratio between κ_1 and κ_t must remain constant as stipulated by Gopalaratnam and Shah [26] and Reinhardt [27], as shown in Fig. 5. Typical values for the stiffness degradation parameter [26,27] are presented in Table 1.

FORTRAN routines have been developed to implement the plasticity algorithms defined in Eqs. (1)–(11). To better illustrate the axial behavior of the proposed material model, an interface element (Fig. 6(a)) is subjected to a cyclic axial load (Fig. 7(a)). Following the typical properties of masonry [1], the element is considered to have a normal stiffness $k_n = 82\ \text{N/mm}^3$ and tensile strength $f_t = 0.25\ \text{N/mm}^2$ with a softening energy $G_f^I = 0.018\ \text{Nmm/mm}^2$. The response of this element is shown in Fig. 7(b). As depicted in Fig. 7(a), first monotonic displacement-controlled increments are

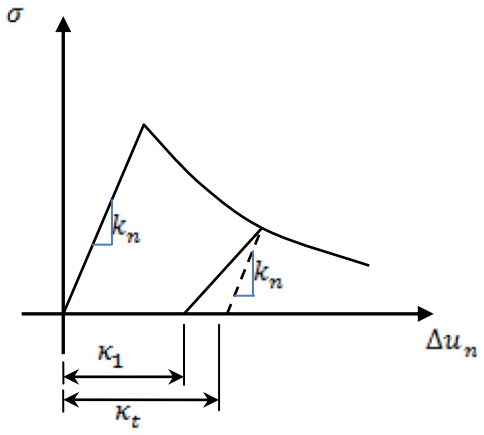

Fig. 5. Cyclic tensile loading [16].

Table 1
Stiffness degradation factor.

Numerical simulation	$\frac{\kappa_1}{\kappa_t}$
Gopalaratnam and Shah [26]	0.76
Reinhardt [27]	0.73

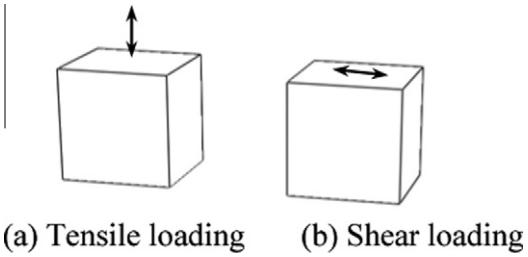

Fig. 6. Interface elements under cyclic loading.

applied up to point "A". Consequently, the normal stress reaches the maximum tensile strength of 0.25 N/mm^2 (see Fig. 7(c)) and the strength degrades following an exponential curve. After load reversal takes place at point "A", the stress decreases with a modified (i.e., degraded) stiffness. Note that the stiffness degradation is only considered for the positive displacements due to the joint closure under the compressive load. Based on the experimental tests conducted by Reinhardt [27] on brittle materials, such as concrete or mortar, the point where the joint closes does not exactly coincide with the zero displacement. However, as a simplification in our approach, it can be considered to be at zero displacement.

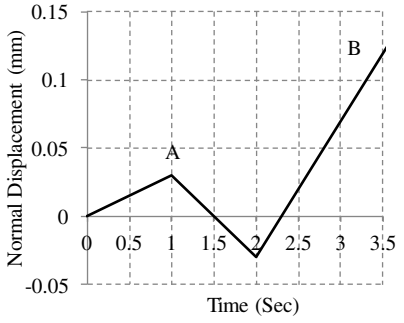

(a) Cyclic normal displacement

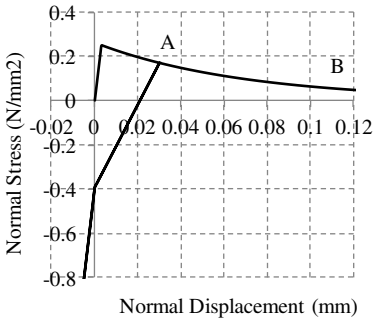

(b) Cyclic normal stress

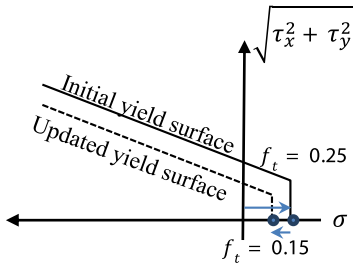

(c) Updating the yield surface

Fig. 7. The results of an element under tensile force.

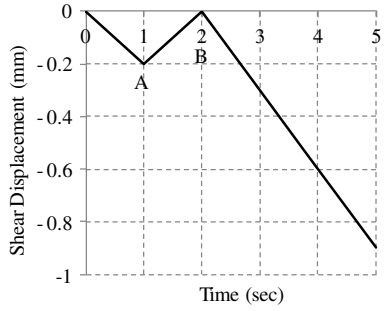

(a) Cyclic shear deformation

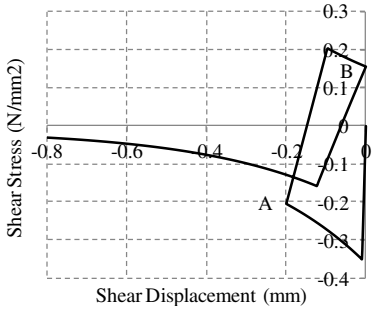

(b) Cyclic shear stress

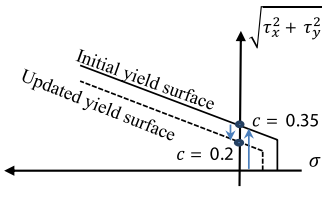

(c) Yield surface

Fig. 8. The results of an element under shear force.

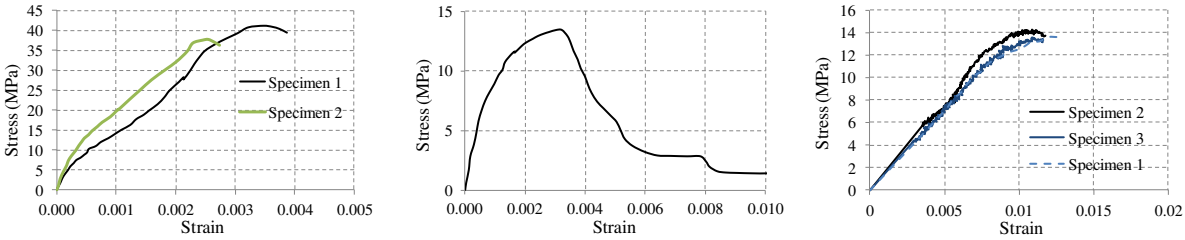

(a) high strength brick (b) low strength brick (c) mortar

Fig. 9. Stress–strain curves.

Fig. 10. The damaged specimen after compression test.

2.2.2. Shear regime

The yield surface for the shear regime follows Eq. (12). The yield surface and nonlinear behavior of the shear-dominated mode is presented in reference [24] for 2D models. Herein, the model is extended to 3D models, and the formulations are derived based on explicit formulations.

$$f_2(\sigma,\kappa_p)=\sqrt{\tau_x^2+\tau_y^2}+\sigma\tan\phi-\bar{\sigma}_2(\kappa_p) \tag{12}$$

$$\bar{\sigma}_2=c\exp\left(-\frac{c}{G_f^{II}}\kappa_p\right) \tag{13}$$

where c is the cohesion of the brick–mortar interface, ϕ is the friction angle, and G_f^{II} is the mode-*II* fracture energy (the area under stress–transverse displacement curve) appearing in Eqs. (12) and (13). In Eq. (12), the friction angle is coupled with cohesion softening,

$$\tan\phi=\tan\phi_0+(\tan\phi_r-\tan\phi_0)\frac{c-\bar{\sigma}_2}{c} \tag{14}$$

where ϕ_0 is the initial friction angle and ϕ_r is the residual friction angle. The flow rule follows the non-associated plastic potential of,

$$g_2=\sqrt{\tau_x^2+\tau_y^2}+\sigma\tan\psi-c \tag{15}$$

where ψ represents the dilatancy angle. Similar to Eq. (10), by employing the normality rule and considering the fact that in the nonlinear regime the state of stress remains on the yield surface, the stress correction factor is calculated by

$$d\lambda=\frac{\tan\psi\ k_n du+\frac{\tau_x}{\sqrt{\tau_x^2+\tau_y^2}}k_{sx}dv_x+\frac{\tau_y}{\sqrt{\tau_x^2+\tau_y^2}}k_{sy}dv_y}{\frac{c^2}{G_f^{II}}exp\left(-\frac{c}{G_f^{II}}\kappa_p\right)-\left(\tan^2\psi\ k_n+\frac{\tau_x^2}{\tau_x^2+\tau_y^2}k_{sx}+\frac{\tau_y^2}{\tau_x^2+\tau_y^2}k_{sy}\right)} \tag{16}$$

Using the plasticity rules and following explicit formulations, the modified stresses at step $i+1$ can be calculated using Eq. (17),

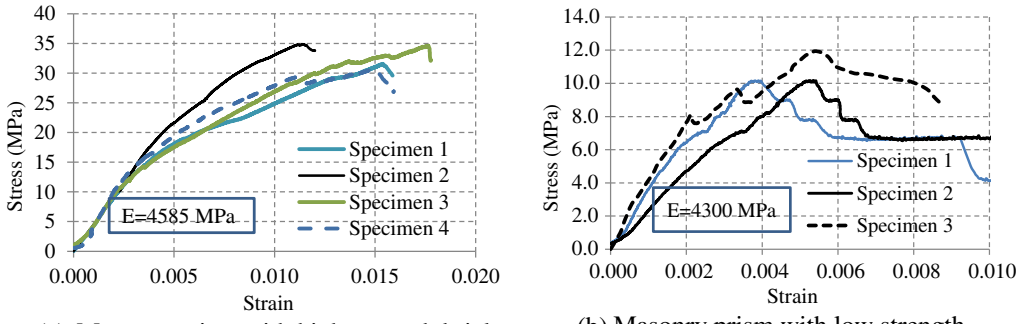

(a) Masonry prism with high strength bricks (b) Masonry prism with low strength bricks

Fig. 11. Stress–strain curves masonry prism specimens.

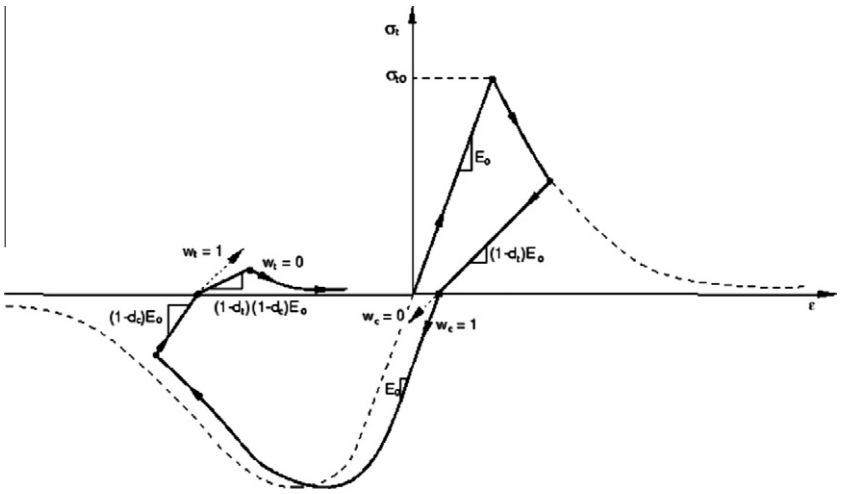

Fig. 12. Concrete damage material model under uniaxial tension and compression test [19].

which accounts for fully updated state of stress in normal and transverse directions

$$\begin{cases} \sigma_{i+1} = \sigma^{trial} - d\lambda\ k_n \tan(\psi) \\ \tau_{x_{i+1}} = \tau_x^{trial} - d\lambda\ k_{sx} \frac{\tau_x}{\sqrt{\tau_x^2+\tau_y^2}} \\ \tau_{y_{i+1}} = \tau_y^{trial} - d\lambda\ k_{sy} \frac{\tau_y}{\sqrt{\tau_x^2+\tau_y^2}} \end{cases} \tag{17}$$

As an example intended to illustrate the behavior of the proposed material model, consider an interface element, shown in Fig. 6(b), that is subjected to a transverse cyclic deformation without the compressive loading (Fig. 8(a)). Following typical values for masonry [1], the calculated element properties are: a transverse stiffness $k_s = 36\ \text{N/mm}^3$ and shear strength $c = 0.35\ \text{N/mm}^2$ with a softening energy $G_f^{II} = 0.125\ \text{Nmm/mm}^2$. Shear stress has been plotted against cyclic transverse displacement in Fig. 8(b). One can see as soon as the shear stress reaches the initial yield surface – which coincides with the value of $0.35\ \text{N/mm}^2$ depicted in Fig. 8(c) – the exponential strength degradation starts to govern the behavior until the loading reversal takes place at point "A". At point "A" the shear strength has reached a reduced value of $0.2\ \text{N/mm}^2$ based on the governing yield surface. In the load reversal, the absolute value of the stress decreases with the degradation of stiffness until the shear stress intersects the updated yield surface ($0.2\ \text{N/mm}^2$ – see Fig. 8(c)). Again, the strength degradation continues until the second load reversal reaches point "B". In Fig. 8(b), stiffness and strength degradation are evidently clear at different stages of the loading. Note that in this numerical simulation no compressive force exists; therefore, the frictional force is not activated.

Experimental results [16] indicate no stiffness degradation for frictional resistance, when a joint is subjected to cyclic transverse loading in the absence of cohesion. In contrast to the tensile strength case and according to Mohr–Coulomb rule, the shear strength is a combination of cohesion and friction. Therefore, for the formulation of stiffness degradation in the transverse cyclic loading, we assume that for the portion of the shear strength where cohesion is involved, the stiffness degradation is similar to that used for tension (Fig. 5). Whereas, for the portion where friction exists, stiffness degradation is not considered. Hence, for the final value of the transverse stiffness, at each time step the average of the two values should be calculated. In other words, for a situation similar to Fig. 8(b) where compressive load does not exist, a formulation similar to the tension-dominated case is used. For an element with a high compressive load, where the frictional force is predominant, no stiffness degradation is considered.

2.2.3. Shear and tension interaction regime

The cohesion behavior of the joint is coupled in tension and shear, since both have the same source, which comes from the cementation of the mortar. Therefore, in the model presented herein, isotropic softening is assumed for the coupled behavior between the shear and tension, similar to the approach adopted by Lourenco [1]. In other words, after applying tensile force and reducing tensile strength to $m\%$ of its initial strength ($0 < m < 100$), the shear strength is also assumed to be reduced by $m\%$ of its initial strength. Therefore, in the formulation, for the total motion in the tensile direction in each time step, the reduction of the tensile strength and the ultimate shear strength are reduced consistently. This is shown as [1]

$$\kappa_{2,n+1} = \frac{G_f^I}{G_f^{II}} \frac{c}{f_t} |\Delta u_n^p| \tag{18}$$

Therefore, for deformations in the shear and tensile direction:

$$\kappa_1 = (\Delta u_n^p) + \left(\frac{G_f^I}{G_f^{II}} \frac{c}{f_t} |\Delta u_n^p| \right) \tag{19}$$

$$\kappa_2 = (\Delta u_s^p) + \left(\frac{G_f^{II}}{G_f^I} \frac{f_t}{c} |\Delta u_n^p| \right) \tag{20}$$

2.2.4. Cap regime for the yield surface

In old buildings and due to the aging of materials, mortar is very weak (usually weaker than bricks). Therefore, there is a possibility for the mortar to fail under compressive forces before the adjoining bricks. An experimental study (uniaxial compressive test) has been performed by the authors, to identify the necessity of using cap regime for the yield surface of the mortar under high compression forces, especially when mortar is very weak. Two different types of bricks have been selected with two different levels of compressive capacities, including a high strength brick and a low strength brick, to construct masonry prism samples. In constructing masonry prisms, only one type of mortar has been used (type "N") for both types of the bricks. The stress–strain curves of uniaxial compression test for high and low strength bricks in addition to the cubic mortar samples are presented in Fig. 9. The high strength

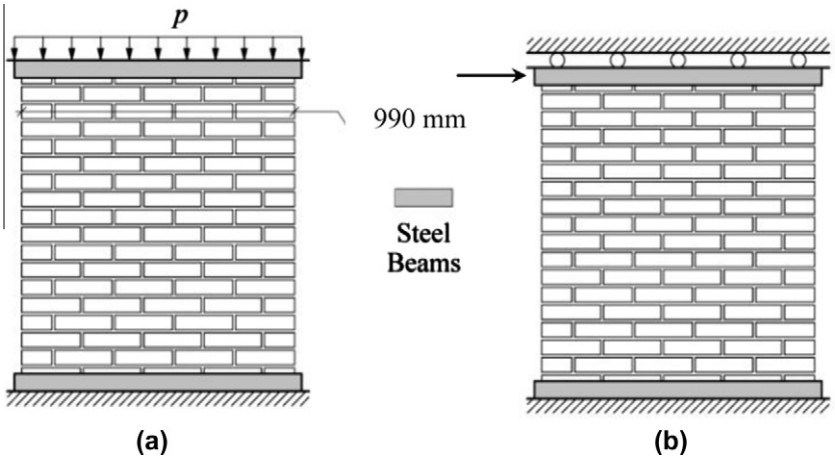

Fig. 13. Steps 1 and 2 for applying the load [1].

Table 2
Properties of different types of crack (J4D/J5D). (Based on the experimental result by [21,22]).

Type	k_n (N/mm^3)	k_s (N/mm^3)
Vertical/horizontal joints	82	36
Potential cracks	1000	1000

brick was about three times stronger than the low strength brick and the mortar as shown in Fig. 9.

Fig. 10 shows a damaged brick prism after uniaxial compression test. For both types of bricks, it was observed that even though the bricks (for high strength bricks) were stronger than the mortar, only bricks were crushed and the mortar was extracted without any significant damage. The reason for this behavior is attributed to the small thickness of the mortar and the high level of confinement of the mortar induced by the adjacent bricks.

The stress–strain curves of the masonry prisms constructed with high and low strength bricks are presented in Fig. 11(a) and (b), respectively. Based on Fig. 11(a) the strength of the masonry prism constructed using high strength brick was three times

Table 3
Inelastic properties of the joints (J4D/J5D). (Based on the experimental result by [21,22]).

Type	Tension		Shear			
	f_t (N/mm^2)	G_f^I(N/mm)	c (N/mm^2)	tan ϕ	tan ψ	G_f^{II}(N/mm)
Vertical/horizontal joints	0.25	0.018	0.35	0.75	0.0	0.125
Potential cracks	2	0.08	2.8	0.75	0.0	0.55

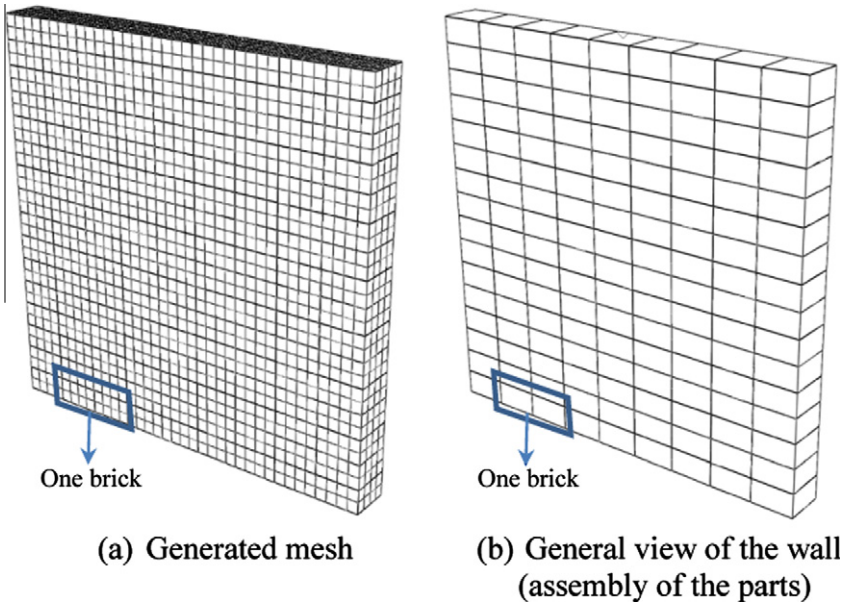

Fig. 14. Numerical modeling of a masonry wall.

greater than the strength of the cubic mortar sample used between the bricks. These observations indicate that no cap regime should be defined in the yield surface of the mortar if the brick is modeled using elasto–plastic elements.

2.3. Nonlinear behavior of the brick elements

The concrete damaged plasticity material model in ABAQUS was used to model the nonlinear behavior of the bricks. This material model is specifically written for concrete. However, it can be used for other quasi-brittle materials including bricks. The model assumes that the main two failure mechanisms for brittle materials are tensile cracking and compressive crushing. In this material model, the position of the yield surface is always controlled by two hardening variables, $\varepsilon_t^{pl}, \varepsilon_c^{pl}$, tensile and compressive plastic strain, respectively. This material behavior is also formulated to capture the cyclic behavior of brittle material by considering stiffness degradation (Fig. 12 – for more information the reader is referred to Ref. [19]).

3. Explicit dynamic analysis

Explicit analysis has been mostly used to solve the equations of motion, either in dynamic or quasi-static problems. In contrast to the implicit procedures, the explicit procedure requires no iterations. The progression of analysis in the time domain is performed by using many small increments dictated by a numerical stability criterion [28].

The explicit dynamic analysis procedure is derived from explicit central difference integration scheme. In order to have a stable numerical solution, the time increment is the only constraint that must be controlled; this parameter should be checked with the highest natural frequency of the system. In other words, to have a conditionally stable central difference operator, the time increment (Δt) should be less than the stability limit (Δt_{max}). In ABAQUS, by using the highest eigenvalue in the system (ω_{max}), the time increment is estimated by using the following inequality [19]:

$$\Delta t \leqslant \frac{2}{\omega_{max}}\left(\sqrt{1+\zeta^2}-\zeta\right) \tag{21}$$

where ζ is the corresponding fraction of the critical damping in the highest mode. Alternatively, this limit can be estimated from the element characteristic dimension L_e and the current effective wave velocity C_d as follows:

$$\Delta t_{max} \leqslant \frac{L_e}{C_d} \tag{22}$$

where $C_d = \sqrt{\frac{E}{\rho}}$, ρ is the density and E is the modulus of elasticity. In nonlinear analysis, by changing the modulus of elasticity, the stability limit will change. A complete discussion of the explicit dynamic function can be found in ABAQUS manual [19].

4. Numerical validations

To validate the proposed constitutive material model, in this section three different numerical simulations are presented with different loading protocols along different directions, and compared to well documented experimental results. The numerical simulations include, (1) in-plane (IP) monotonic loading (2) out-of-plane (OP) monotonic loading, and (3) combination of IP and OP cyclic loading.

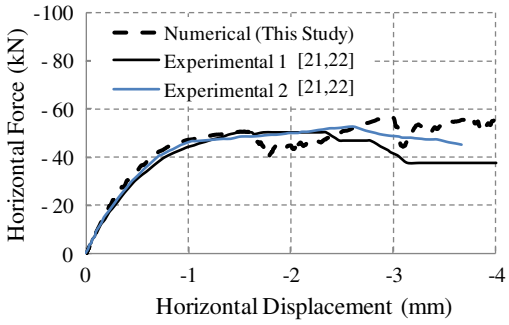

Fig. 15. Comparison of numerical and experimental load–displacement curves.

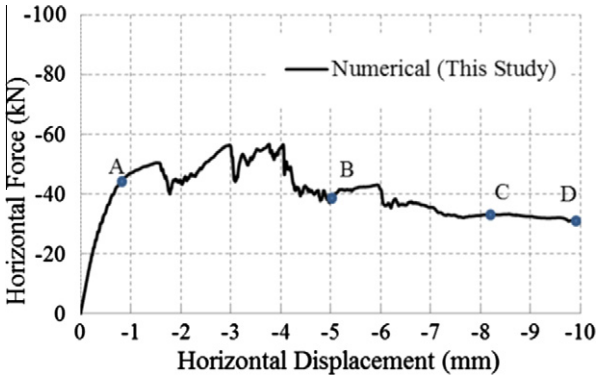

Fig. 16. Numerical load–displacement curve.

4.1. In-plane monotonic loading

The experimental and well-documented results by Raijmakers and Vermelfoort [21] and Vermelfoort and Raijmakers [22] were used to verify the proposed constitutive material model under monotonic in-plane loadings. Vermelfoort and Raijmakers performed an experimental study on two masonry walls with the same geometry. The walls (wall J4D and wall J5D) were subjected to an identical compressive loading of 30 kN. The height and width of the walls were 1,000 and 990 mm, respectively, and had 16 active rows of brick. The dimensions of the bricks were $210 \times 52 \times 100$ mm and the mortar was 10 mm thick, prepared with a volumetric cement:lime:sand ratio of 1:2:9 (Fig. 13). The compressive load was applied first (Fig. 13(a)) then the vertical displacement of the top surface was constrained. A monotonic displacement-controlled load was finally imposed horizontally on top of the wall (Fig. 13(b)).

Different experimental tests were also performed to obtain the properties of the mortar and bricks [21,22]. The authors did not have complete access to the material properties of the bricks used in the concrete damaged material model of ABAQUS. Typical material properties were selected from a range provided by Stavridis [29] for bricks with compressive strength of 10.5 N/mm^2. Therefore, the tensile strength of the masonry units is assumed to be 10% of its compressive strength with the mode-*I* fracture energy of 0.105 N/mm.

The FE model of the wall was created according to the description of Section 2 and using the material properties given in Tables 2 and 3. Fig. 14(a) and (b) shows the generated FE mesh for the wall and a general view of the numerical model of the wall, respectively. The size of the brick elements in this model is about $2.5 \times 2.5 \times 2.5$ cm. Fig. 14(b) shows the assembly of the parts (half bricks and joints) in the finite element software. As indicated earlier and shown in Fig. 14(b), an interface element is located in the

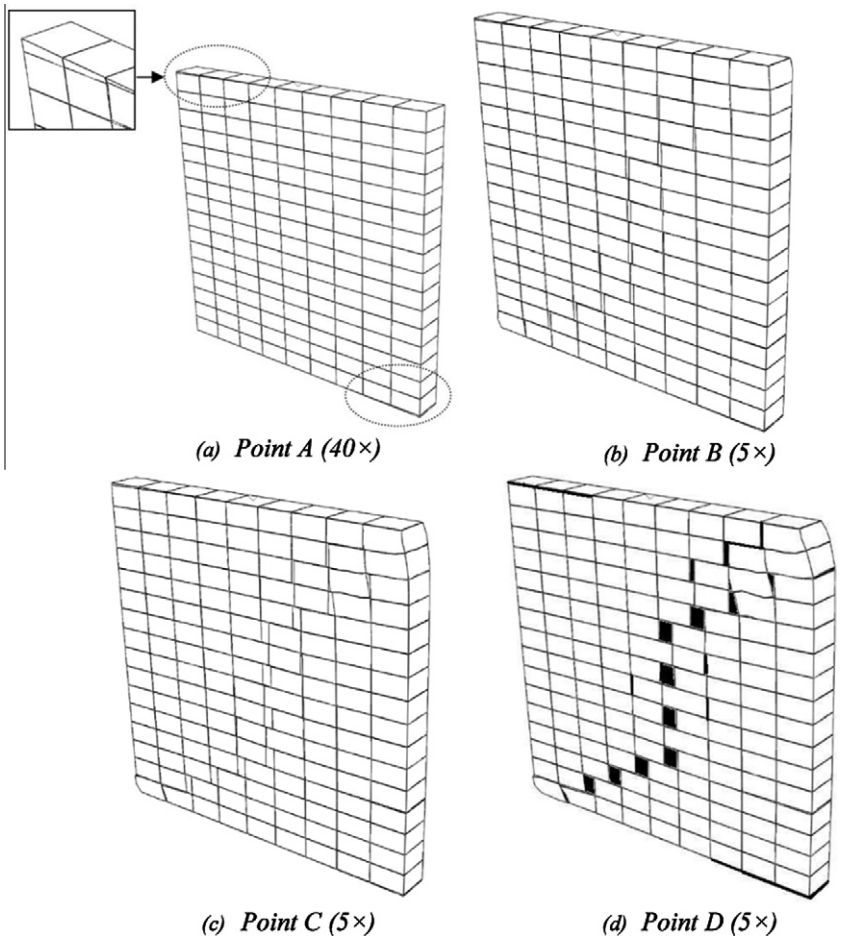

Fig. 17. Crack pattern of the wall at different stages of loading; note that mesh is turned off in this view.

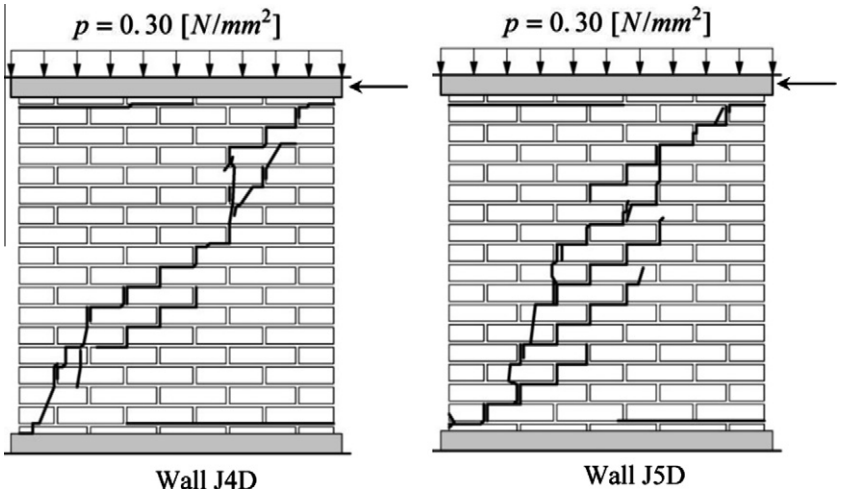

Fig. 18. Experimental crack pattern at 4 mm displacement [1].

middle of the bricks to better simulate the crack propagation of the bricks.

After imposing the compressive load on the top plane of the wall, the vertical deformation of the top plane of the wall was restrained. To impose the horizontal loading in Fig. 13, two different approaches can be considered. Numerical modeling can be performed by using either quasi-static or dynamic analysis. In this paper, the latter procedure is employed to show the capabilities of the model in dynamic simulations. Thus, by applying a constant velocity at the top plane of the wall, a monotonic deformation was imposed to the wall. In Fig. 15, the dashed line represents the solution obtained using the proposed constitutive material model and numerical procedure and the two solid lines correspond to the experimental results.

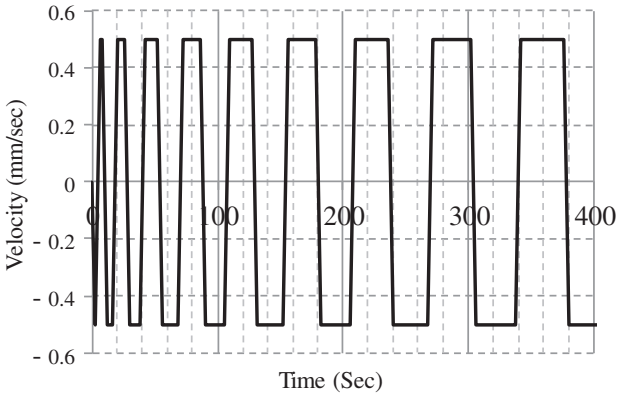

Fig. 19. Cyclic velocity applied at the top plane of the wall.

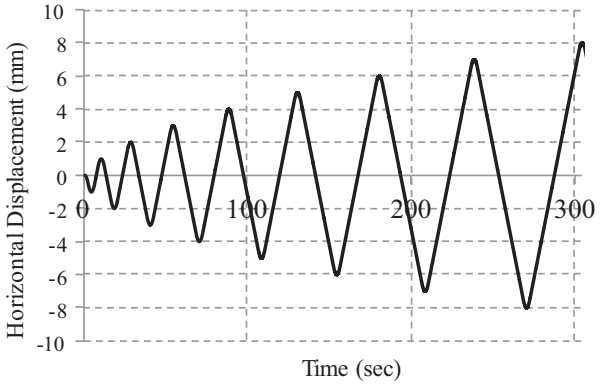

Fig. 20. Resulting cyclic displacement at the top plane of the wall.

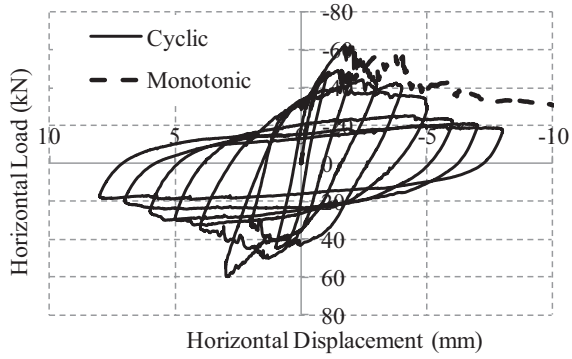

Fig. 21. Cyclic load–displacement curve.

Fig. 16 shows the numerical results for 10 mm horizontal displacement. As expected, after the diagonal crack completed, the wall continued to resist the loading by the frictional force at the cracked surfaces, which is evident by the horizontal force remaining almost unchanged after 6 mm, as shown in Fig. 16. Using the proposed constitutive model and the associated numerical algorithms, it is possible to simulate large displacements. However, to obtain more accurate results for large displacements, a very fine mesh should be used to allow the accurate creation of cracks and formation of new contacts. The mesh sensitivity of the numerical model is reported by Dolatshahi [13].

The crack pattern at different stages of loading is shown in Fig. 17. To indicate the path of the crack in the early stages of loading, different magnification factors are used for each snapshot. In the first figure, the displacement is magnified 40 times (40×), but in the last three figures where the deformations are higher, a magnification factor of five (5×) is used. Fig. 17 shows that initially the crack propagated from the two corners and continued to a full diagonal crack. We note here also that the points at which the crack patterns are obtained are marked in Fig. 16.

Fig. 18 shows the experimental crack pattern at a displacement of 4 mm. It is abundantly clear that even for two walls with the same material properties and loading, the experimental crack patterns are distinctly different. This deviation is primarily due to the heterogeneity of the mortar and brick materials. We evidently show that the numerical crack pattern and load–displacement response are in good agreement with the experimental results.

As the second phase of numerical modeling, a cyclic loading was applied to the same wall used in the first example. To obtain the cyclic loading protocol of Fig. 20, a varying velocity was applied at the top plane of the wall according to Fig. 19.

The numerical simulation results of the cyclic loading along with the monotonic loading are shown in Fig. 21. In this figure, strength and stiffness degradation are clearly evident. After a few cycles, as depicted in Fig. 21, the frictional force that is associated with some strength degradation governs the cyclic response. The top plane of the wall is constrained in the vertical direction while the horizontal force was applied; therefore, after crushing of the bricks located at the corners, the total compressive load decreases and subsequently the resisting frictional force decreases. This is one of the reasons that the resisting force decreases in the cyclic loading depicted in Fig. 21.

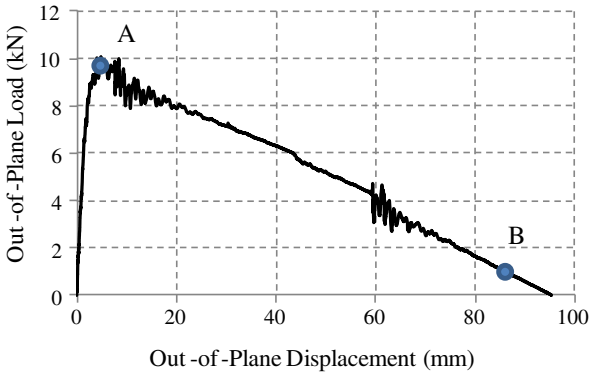

Fig. 22. Load–displacement curve for the out-of-plane direction loading.

4.2. Out-of-plane loading on masonry walls

In this section, the masonry wall discussed in the previous section is subjected to a monotonic out-of-plane displacement. The boundary conditions are the same as the examples in the previous section, except for the top plane which is not constrained in the vertical direction. Fig. 22 shows the load–displacement of the wall under monotonic out-of-plane loading. This figure illustrates that after a specific out-of-plane deformation (about 100 mm) the wall become unstable.

The deformed configuration of the wall under out-of-plane loading in points "A" and "B" of Fig. 22 is presented in Fig. 23. Point "A" shows the configuration of the wall when it has the most resisting force and point "B" corresponds to the point where the wall will be unstable at the larger deformation than deformation of point "B". As shown in Fig. 23, most of the damage is associated with the top and bottom three rows of the mortar in the wall. As the deformation of the wall increases from point "A" to point

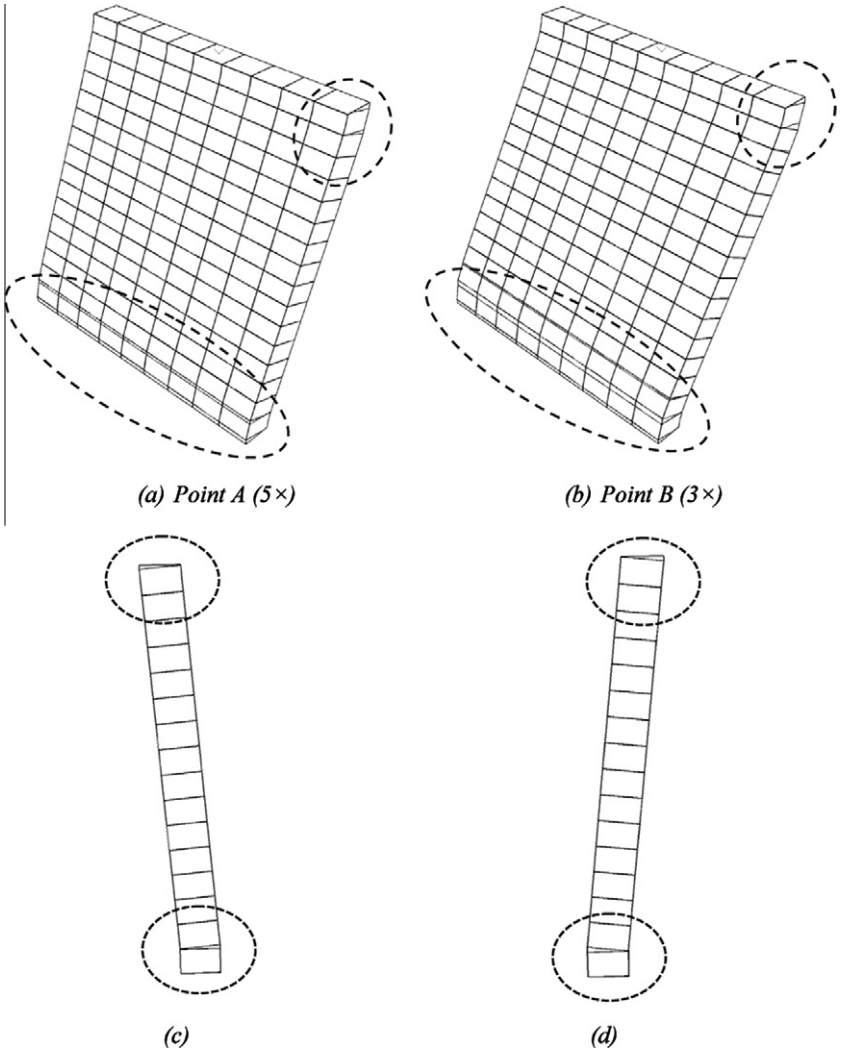

Fig. 23. Deformed configuration of the wall under out-of-plane loading; note that mesh is turned off for clarity.

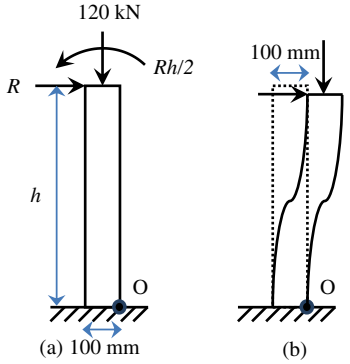

Fig. 24. Moment diagram for OP load.

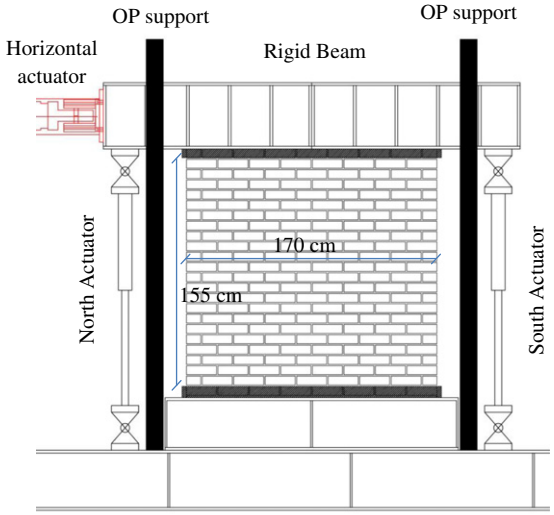

Fig. 25. Testing set up.

"B", more crack opening is exhibited at point "B". In Fig. 23(c) and (d) the wall is subjected to cyclic out-of-plane loading. Fig. 23(c) and (d) show the deformed shape (rocking) of the wall under out-of-plane cyclic loading. The circular dashed lines in Fig. 23 show a close-up at the crack opening of the mortar at the end of the cycles. This figure clearly indicates the correct functionality of the discussed material model in the simulation of opening and closing of the joints.

Fig. 24 presents the moment diagram of the wall under OP loading. According to Fig. 24(a), by writing the moment equilibrium equation under point "O", the maximum value of the resisting

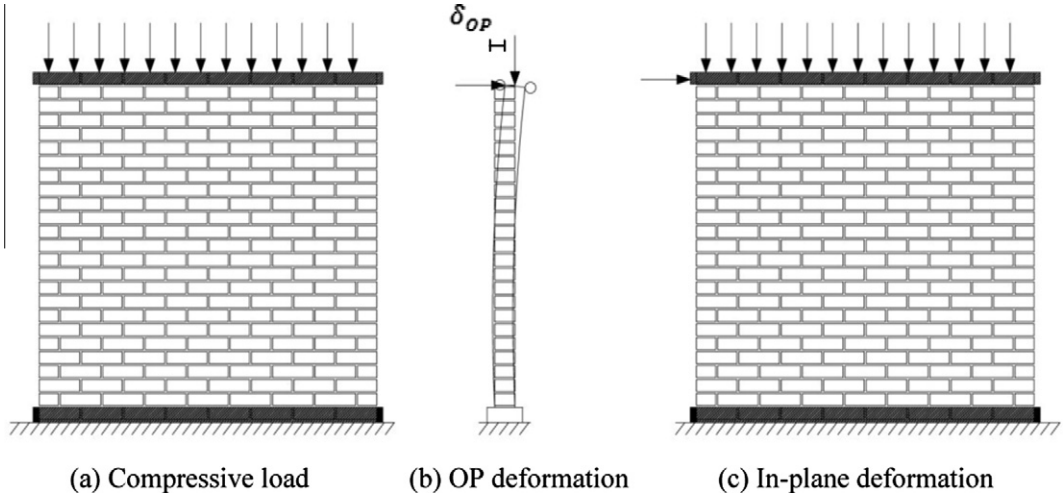

Fig. 26. Combination of IP and OP loadings.

Table 4
Material properties of the brick.

Elastic		Compressive			Tensile		
E (N/mm^2)	v	f_c (N/mm^2)	κ_p	κ_m	f_t'(N/mm^2)	G_f^I(N/mm)	G_f^{II}(N/mm)
26500	0.15	34.5	0.007	0.0115	3.5	0.13	1.3

Table 5
Joint properties.

Elastic		Shear				Tension	
k_n (N/mm^3)	$k_{sx,y}$ (N/mm^3)	tan Ø	tan ψ	c (N/mm^2)	G_f^{II}(N/mm)	f_t (N/mm^2)	G_f^I(N/mm)
62	27	0.92	0.0	0.135	0.0625	0.1	0.00625

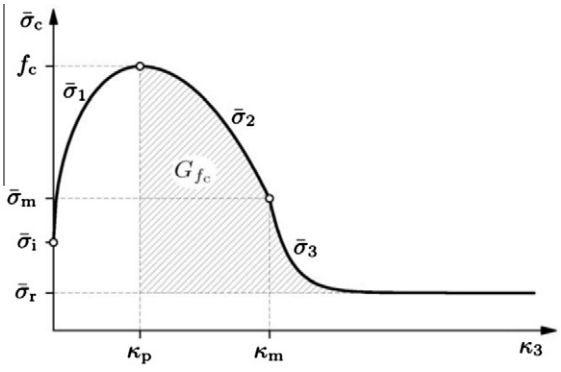

Fig. 27. Idealized stress–strain curve under uniaxial compression test.

force (R) can be calculated. Note that, based on Fig. 23(a) in the deformation associated to the maximum OP force (point "A" in Fig. 22), the top and bottom planes are already separated from the supports and mortar cohesion does not contribute in the OP resisting force.

$$\Sigma M_O = 120(50-\Delta) + \frac{R\ 1000}{2} - R\ 1000 = 0 \tag{23}$$

where Δ represents the OP deformation of the wall associated to the maximum OP resisting force. According to Fig. 22 and point "A", for $\Delta = 7$ mm Eq. (21) yields $R = 10.3$ kN which is very close to the finite element results presented in Fig. 22.

As shown in Fig. 24(b) after about 100 mm out-of-plane deformation, the top and bottom planes do not have any overlap and the wall losses its stability under the gravity load. This conclusion is in accord with the finite element results in Fig. 22 (point "B").

4.3. Combination of IP and OP cyclic loading

An experimental study has been conducted by the authors to investigate the interaction behavior of the masonry walls under in-plane and out-of-plane loadings. A brief description of the test is presented in the following sections. For more information refer to Ref. [13].

A masonry wall with 23 rows of brick has been constructed with the width and height of, 170 and 155 cm, respectively; in building the wall type "*N*" mortar has been utilized and the bricks had the same dimensions of 20.3, 10, 6 cm in width, thickness and height, respectively. Attention was paid to maintaining the dimension of the mortar constant at 1 cm in all horizontal and vertical joints (see Figs. 25 and 26). According to Fig. 25 two vertical actuators applied the axial load to the wall that represents the gravity load, and a horizontal actuator applied the deformation-controlled horizontal load. The vertical actuators applied the axial load to the rigid beam and the rigid beam distributed the load to the top plane of the wall. As shown in Fig. 25 four vertical columns were assigned as an OP support to control the OP deformation of the wall.

The wall has been tested in the IP direction with a combination of an OP deformation. In the first step of loading, the compressive load was applied on the top plane of the wall (100 kN, see Fig. 26(a)), afterward, while keeping the compressive load

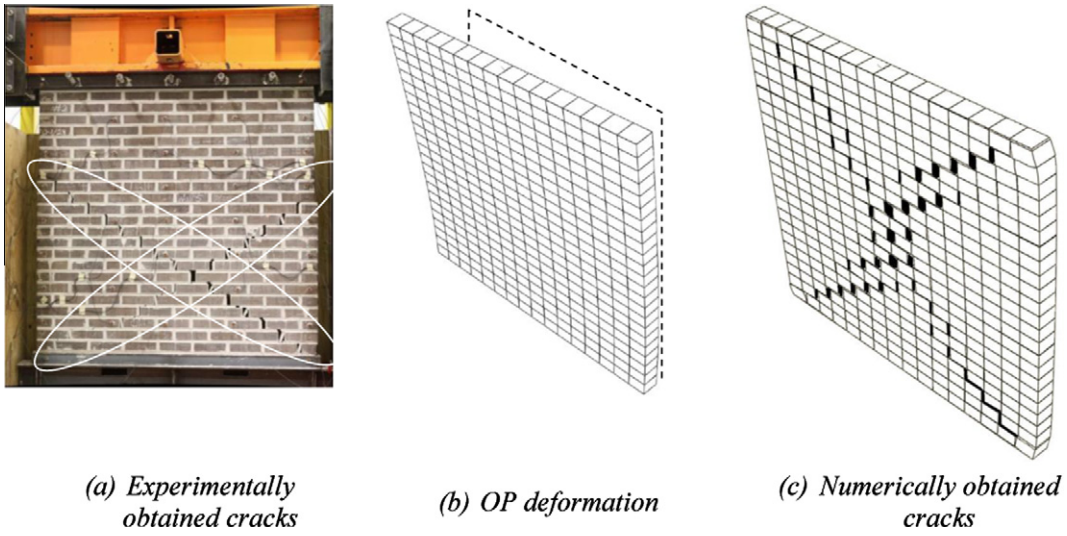

Fig. 28. Comparison between numerical and experimental cracks.

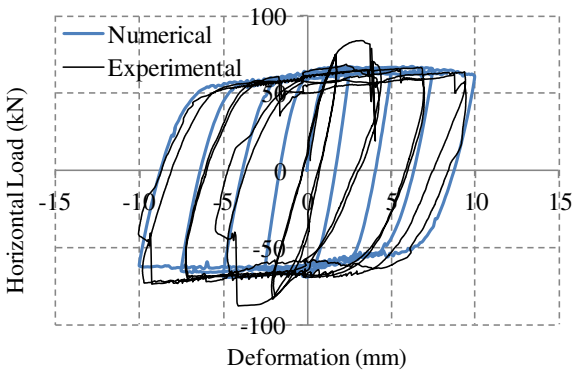

Fig. 29. Comparison of experimental and numerical load displacement curves.

constant, an OP deformation (δ_{OP}) of 10 mm was imposed to the wall (Fig. 26(b)). Then, using two rollers beside the rigid beam at top plane of the wall, the boundary condition has been imposed to the rigid beam in such a way that any OP deformation of the rigid beam was kept at the imposed value of 10 mm (Fig. 26). Finally a displacement-controlled cyclic loading has been applied to the top plane of the wall in the IP direction. Throughout the testing the controller distributed the vertical load in two vertical actuators in such a way that the rigid beam remained level.

The mechanical properties of different materials were obtained by the authors and presented in Table 4 and 5. The elastic properties of the joints are calculated according to Eqs. (4) and (5). As shown in Fig. 27, a combination of three functions have been used to show the stress–strain curve of the brick under uniaxial compression test [1]. This stress–strain curve is used as an input data for the numerical modeling, and specifically for the concrete damaged material model in ABAQUS.

Where f_c, κ_p and κ_m are defined in Fig. 27.

The experimental crack propagation is presented in Fig. 28(a). Fig. 28(b) shows the deformation of the wall obtained from the numerical analysis after the OP displacement was imposed. Following the OP deformation, a cyclic IP displacement-controlled loading has been applied in the numerical model. The resulting crack propagation obtained numerically is presented in Fig. 28(c). As shown in Fig. 28, in both experimental and numerical analysis diagonal crack is the dominant failure mode. We note here that the diagonal crack in the experimental deviates in one aspect and that is the pattern does not reach the corners, but rather at the two-third of the height. One possible explanation is that the quality of the mortar in this region is likely to be higher, as the wall was not constructed in one working day. Moreover, using high precision instruments (such as the Krypton [30] and string pots) in the out-of-plane direction it was observed that the top plane of the wall did not ideally remain at a constant out-of-plane displacement due to the flexibility of the out-of-plane constrains (in contradiction with the numerical model in Fig. 28(b) and (c)). Therefore, the wall experienced a small torsion during the test (detailed information is provided in Ref. [13]).

Due to the high strength of the brick used in the wall, not much nonlinearity has been seen in the bricks, and the nonlinear behavior of the wall was mostly governed by the nonlinearity of the joints.

Fig. 29 compares the experimental and numerical load–displacement results. In the presented numerical results the parameter κ_1/κ_t (stiffness degradation factor) is assumed to have a unit value (see Fig. 5), which implies stiffness degradation is not considered in the mortar. Fig. 29 shows a close agreement between the results of experimental and the numerical simulations.

5. Conclusion

This paper described the development of a robust modeling strategy for simulating the response of masonry structures subjected to 3D loadings. The modeling strategy entails the development of a constitutive material model and its implementation in a user-defined subroutine in ABAQUS.

Several simulations were conducted to evaluate the accuracy and robustness of the derived material model and its implementation at both the element- and structure-level, and the numerical results were compared to several well-documented experimental results obtained by the authors and others.

The following points summarize the conclusions:

- Exponential softening is in good agreement with the behavior of the mortar under tensile or transverse displacements, and such model is well-suited to represent cohesion or tensile strength degradation.
- When using a relatively weak mortar with strong brick, the mortar will not fail under compression primarily due to the high confinement of the thin mortar layer between the adjacent bricks; therefore, no cap regime should be defined for the yield surface of the mortar.

- After failure of the wall in the in-plane direction, the wall continues to withstand the loading by the frictional forces (considering its aspect ratio); whereas, in the out-of-plane direction and due to the low aspect ratio of the tested walls that were governed by the dominance of the rocking behavior, the out-of-plane strength after reaching a peak value diminishes to zero very rapidly.
- In the numerical simulations pertinent to the out-of-plane loading and by comparing to the theoretical results, numerical simulations were able to predict the collapse of the wall, and have traced the theoretical results accurately.
- While several researchers have reported on the convergence issues of implicit models that were used to model masonry structures, the developed material model and its implementation in the user-defined subroutine in ABAQUS have remedied the convergence and stability issues. Furthermore, the modeling strategy offers efficient and a relatively reduced computational demand. More work, however, is still needed to further enhance the computational efficiency of the numerical modeling strategy.

Acknowledgments

Support for this work was provided by MCEER. This support is gratefully acknowledged. Any opinions, findings, conclusions or recommendations expressed in this report are those of the authors and do not necessarily reflect those of MCEER, the State of New York, or other sponsors.

References

[1] Lourenco P. Computational strategies for masonry structures [PhD Dissertation]. Netherlands: Delft University; 1996.
[2] Oliveira DV, Lourenco PB. Implementation and validation of a constitutive model for the cyclic behaviour of interface elements. Comput Struct 2004;82:1451–61.
[3] Oliveira DV, Lourenco PB. Implementation and validation of a constitutive model for the cyclic behaviour of interface elements. Computational Mechanics in Portugal, April 17, 2003–April 19, 2003. 17–19 ed. Portugal, Portugal: Elsevier Ltd; 2004. p. 1451–61.
[4] Gambarotta L, Lagomarsino S. Damage models for the seismic response of brick masonry shear walls. Part i: the mortar joint model and its applications. Earthquake Eng Struct Dyn 1997;26:423–39.
[5] Gambarotta L, Lagomarsino S. Damage models for the seismic response of brick masonry shear walls. Part ii: the continuum model and its applications. Earthquake Eng Struct Dyn 1997;26:441–62.
[6] Casolo S, Pena F. Rigid element model for in-plane dynamics of masonry walls considering hysteretic behaviour and damage. Earthquake Eng Struct Dyn 2007;36:1029–48.
[7] Calderini C, Lagomarsino S. Continuum model for in-plane anisotropic inelastic behavior of masonry. J Struct Eng 2008;134:209–20.
[8] Park J, Towashiraporn P, Craig JI, Goodno BJ. Seismic fragility analysis of low-rise unreinforced masonry structures. Eng Struct 2009;31:125–37.
[9] Senthivel R, Lourenco PB. Finite element modelling of deformation characteristics of historical stone masonry shear walls. Eng Struct 2009;31:1930–43.
[10] Pasticier L, Amadio C, Fragiacomo M. Non-linear seismic analysis and vulnerability evaluation of a masonry building by means of the sap2000 v. 10 code. Earthquake Eng Struct Dyn 2008;37:467–85.
[11] Chen SY, Moon FL, Yi T. A macroelement for the nonlinear analysis of in-plane unreinforced masonry piers. Eng Struct 2008;30:2242–52.
[12] Casolo S. Modelling in-plane micro-structure of masonry walls by rigid elements. Int J Solids Struct 2004;41:3625–41.
[13] Dolatshahi KM. Computational, analytical and experimental modeling of masonry structures [PhD Dissertation]. Buffalo: State University of New York at Buffalo; 2012.
[14] Page AW. Finite element model for masonry. J Struct Div ASCE 1978;104(8):1267–85.
[15] Dolatshahi KM, Aref AJ. Two-dimensional computational framework of meso-scale rigid and line interface elements for masonry structures. Eng Struct 2011;33:3657–67.
[16] Oliveira DV. Experimental and numerical analysis of blocky masonry structures under cyclic loading [PhD Dissertation]. Portugal: University of Minho; 2003.
[17] Karapitta L, Mouzakis H, Carydis P. Explicit finite-element analysis for the in-plane cyclic behavior of unreinforced masonry structures. Earthquake Eng Struct Dyn 2011;40:175–93.
[18] Dhanasekar M, Haider W. Explicit finite element analysis of lightly reinforced masonry shear walls. Comput Struct 2008;86:15–26.
[19] Abaqus. User's manual. Version 6.5: Hibbit and Karlson and Sorensen Inc.; 2005.
[20] Haider W. Inplane response of wide spaced reinforced masonry shear walls. Australia: Central Queensland University; 2007.
[21] Raijmakers TMJ, Vermeltfoort AT. Deformation controlled tests in masonry shear walls. Delft: Report B-92-1156, TNO-Bouw; 1992.
[22] Vermeltfoort AT, Raijmakers. Deformation controlled tests in masonry shear walls, part2. Netherlands: Eindhoven University of Technology; 1993.
[23] Pluijm Vd. Material properties of masonry and its components under tension and shear. In: Neis S VV, Saskatchewan, editors. Proceedings of 6th Canadian masonry symposium. Canada; 1992.
[24] Pluijm Vd. Shear behavior of bed joints. In: Hamid AA, Harris HG, editors. Proceedings of 6th North American masonry conf. USA: Drexel University, Philadelphia, Pennsylvania; 1993.
[25] Lubliner J. Plasticity theory. New York: Macmillan Publishing Company; 1990.
[26] Gopalaratnam VS, Shah SP. Softening response of plain concrete in direct tension. J Am Concrete Inst 1985;82:310–23.
[27] Reinhardt HW. Fracture mechanics of an elastic softening material like concrete. Heron 1984:29.
[28] Bathe K-J. Finite element procedures. 2nd ed. Prentice Hall; 1995.
[29] Stavridis A. Analytical and experimental study of seismic performance of reinforced concrete frames infilled with masonry walls [PhD Dissertation]. San Diego: University of California, San Diego; 2009.
[30] Krypton manual. Leuven, Belgium: Krypton Electronic Engineering n.v.; 2003.